



Revealing multiple classes of stable quantum emitters in hexagonal boron nitride with correlated optical and electron microscopy

Fariah Hayee¹✉, Leo Yu², Jingyuan Linda Zhang³, Christopher J. Ciccarino⁴, Minh Nguyen⁵, Ann F. Marshall⁶, Igor Aharonovich⁵, Jelena Vučković³, Prineha Narang⁴, Tony F. Heinz^{2,7} and Jennifer A. Dionne^{8,9}✉

Defects in hexagonal boron nitride (hBN) exhibit high-brightness, room-temperature quantum emission, but their large spectral variability and unknown local structure challenge their technological utility. Here, we directly correlate hBN quantum emission with local strain using a combination of photoluminescence (PL), cathodoluminescence (CL) and nanobeam electron diffraction. Across 40 emitters, we observe zero phonon lines (ZPLs) in PL and CL ranging from 540 to 720 nm. CL mapping reveals that multiple defects and distinct defect species located within an optically diffraction-limited region can each contribute to the observed PL spectra. Local strain maps indicate that strain is not required to activate the emitters and is not solely responsible for the observed ZPL spectral range. Instead, at least four distinct defect classes are responsible for the observed emission range, and all four classes are stable upon both optical and electron illumination. Our results provide a foundation for future atomic-scale optical characterization of colour centres.

Single-photon emitters (SPEs) in solids have emerged as promising candidates for quantum photonic sensing^{1–3}, communications^{4,5} and computing^{6,7}. Defects in hexagonal boron nitride (hBN) exhibit promising quantum-optical properties, including narrow linewidths^{8–10}, high brightness⁸, high photostability^{11,12} and high emission into the zero phonon line (ZPL)¹³. However, both intrinsic and engineered defects in mono- and multilayer films exhibit large spectral variability^{14–16}. Additionally, some emitters exhibit distinct polarization profiles for absorption and emission¹⁷ as well as distinct quantum efficiencies for different excitation wavelengths, suggesting a complicated electronic structure^{11,12,18}. Strain has been postulated to be responsible for such spectral variability¹⁰, where density functional theory calculations have predicted multiple defect structures as candidates^{19,20}. However, the origin of the reported spectral variability of single-photon emitters remains unknown. Establishing a correlation between the emission of an SPE and its local crystallographic environment is a necessary step towards defect identification and application in various quantum technologies.

Recent progress in super-resolution optical microscopy and cathodoluminescence (CL) spectroscopy has enabled localization of radiative emission beyond the diffraction limit. For example, quantum emission from hBN has been visualized with 10-nm and 80-nm spatial resolution using super-resolution techniques²¹ and CL spectroscopy^{22,23}, respectively. However, to date, these techniques have not provided a one-to-one correlation between emission and any structural property, including strain and defect structure. In parallel, aberration-corrected electron microscopy^{24,25} and scanning

tunnelling microscopy^{26–28} have revealed individual defect structures in mono- and multilayered materials, but without correlation to the optical signatures of the defects. Notably, locating SPEs within an electron microscope can be extremely challenging, since most samples possess a small density of visible SPEs. Furthermore, most transmission electron microscopes (TEMs) lack optical excitation and detection capabilities, and the effect of the electron beam on single-photon-emitting defects remains unknown.

Here, we correlate the photoluminescence (PL) and CL spectroscopic signatures of hBN visible-frequency SPEs with their local strain using scanning transmission electron microscopy (STEM). First, we establish a direct correlation between the PL and CL emission of an SPE, showing two classes of stable emitters: those for which both electron-beam excitation and 532-nm laser excitation generate the same emission spectra, and those for which CL peaks are spectrally shifted. We then use hyperspectral STEM-CL mapping and find that multiple radiative defects are localized within a ~50-nm region. Accordingly, defect-defect interactions and/or multiple radiative transitions within the joint density of electronic states can influence the far-field PL spectra. Using high-resolution electron imaging, we find that about 30% of the studied emitters are positioned at least 12 nm away from any possible flake edges. Then, using nanobeam electron diffraction, we measure strain variations in the ~20-nm regions surrounding the SPEs. A number of SPE wavelengths are observed without considerable strain variation, indicating that strain is not solely responsible for the observed spectral variability. Importantly, our results show that emitters can be classified into at least four distinct SPE defect species,

¹Department of Electrical Engineering, Stanford University, Stanford, CA, USA. ²Department of Applied Physics, Stanford University, Stanford, CA, USA.

³E. L. Ginzton Laboratory, Stanford University, Stanford, CA, USA. ⁴John A. Paulson School of Engineering and Applied Sciences, Harvard University, Cambridge, MA, USA. ⁵School of Mathematical and Physical Sciences, University of Technology Sydney, Ultimo, New South Wales, Australia. ⁶Stanford Nano Shared Facilities, Stanford University, Stanford, CA, USA. ⁷SLAC National Accelerator Laboratory, Menlo Park, CA, USA. ⁸Department of Materials Science and Engineering, Stanford University, Stanford, CA, USA. ⁹Department of Radiology, Stanford University, Stanford, CA, USA.

✉e-mail: fariah@stanford.edu; jdionne@stanford.edu

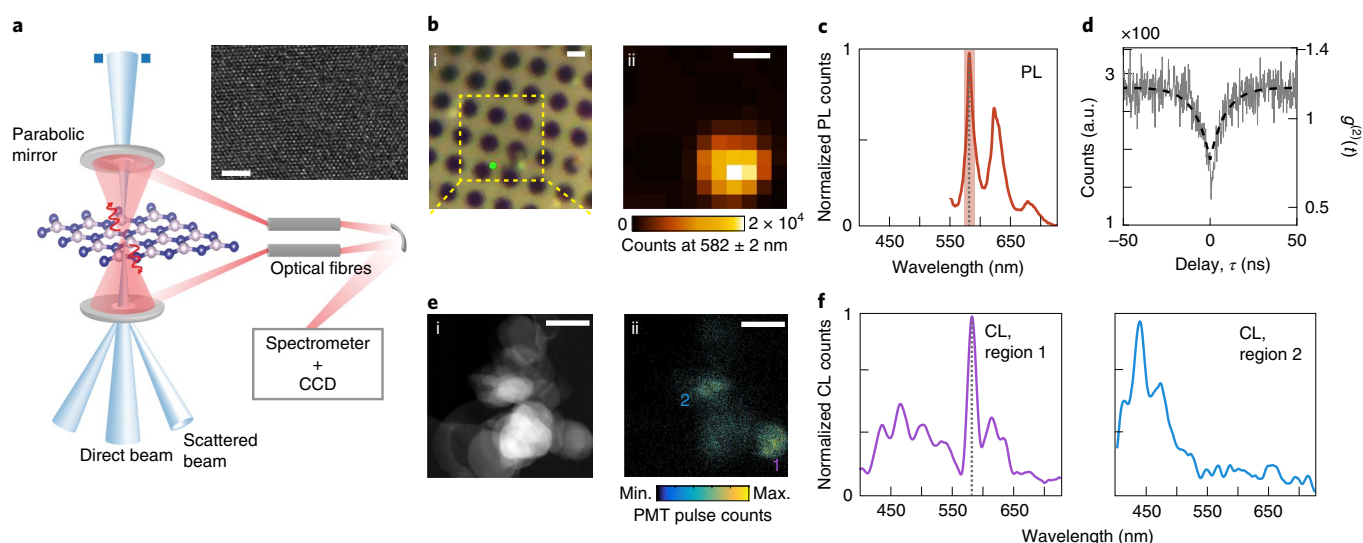


Fig. 1 | Correlated optical and electron characterization of quantum emitters in hBN. **a**, Schematic illustration of the cathodoluminescence set-up in a TEM. Two parabolic mirrors surround the sample and the resulting signal is collected via optical fibres and directed to a spectrometer. An alternative light path to a photomultiplier tube (not shown) can be selected by changing the mirror position. The inset shows a high-resolution TEM image of the sample. Scale bar, 2 nm. **b**, Optical image (i) and photoluminescence map for emission at 582 nm (ii) from a hBN sample on a holey carbon TEM grid. Scale bars, 1 μm . **c**, PL spectrum at the optical hotspot. **d**, Unnormalized photon coincidence counts for the emitter, with the right y axis showing the normalized $g^{(2)}$ counts; the black dashed line is fitted with a three-level model. The vertical shaded area in the PL spectrum corresponds to the ZPL studied. **e**, STEM-HAADF image (i) and panchromatic-CL map (ii) of the same hBN flake as in **b**. Scale bars, 200 nm. **f**, CL spectra of the two regions marked in **e**(ii).

with each species responsible for the 580, 615, 650 and 705 nm spectral regions.

Correlation of photo- and cathodoluminescence spectra

Our experimental STEM-CL set-up is depicted in Fig. 1a. A hBN multilayer (1–5 layers) nanoflake solution in ethanol and water is drop-cast onto a holey carbon TEM substrate for PL, CL and TEM imaging. First, we identify emission centres in multilayer hBN flakes using confocal PL mapping with a 532-nm excitation laser. With this sub-bandgap excitation²⁹, we excite defects lying deep in the bandgap. We find bright emission ranging between 540 and 720 nm, with spectral full-width at half-maximum (FWHM) values ranging from 4 to 12 nm at room temperature. Figure 1b,c includes an optical micrograph, PL map and PL spectrum of one such representative emitter, with a ZPL at 582 nm and two phonon replicas at 622.5 and 680.7 nm (separated by 139 and 161 meV from the ZPL). We verify that the emission lines are indeed of single-photon nature by characterizing the second-order autocorrelation function $g^{(2)}(\tau)$ using a Hanbury Brown–Twiss (HBT) set-up. Despite the high background contribution at room temperature, the zero-delay ($\tau=0$) dip in the unnormalized coincidence count in Fig. 1d is indicative of the dominant emission from non-classical emitters. The $g^{(2)}(\tau)$ on the right y axis of Fig. 1d, which is estimated on the basis of the coincidence count at 4 μs , can be an overestimation due to longer delay time (>4 μs) bunching effects observed in hBN emitters^{12,30}. Additional emitters with $g^{(2)}(0)$ well below 0.5 are included in the Supplementary Information; the similarity between our observed PL spectra and those of the reported hBN quantum emitters^{8,9,30} further supports the non-classical nature of the emitters that we studied.

We next identify the same emitters in the TEM (see Methods). The process of light generation in CL is incoherent: electrons excite a high-energy bulk plasmon (~ 20 eV for hBN), which decays within a femtosecond time period to generate multiple electron–hole pairs²². As shown in Fig. 1a, we use a focused electron probe (typical diameter of 1.5 nm) and collect the emitted light using two parabolic mirrors positioned above and below the sample. A spectrometer

and CCD (charge-coupled device) enable spectroscopic mapping of defects correlated with high-resolution transmission electron microscopy. An alternative light path with a photomultiplier tube (PMT) is used to rapidly map panchromatic emission. A high-angle annular dark-field (HAADF) image and corresponding panchromatic-CL (pan-CL) image are shown in Fig. 1e. The HAADF image shows multiple overlapping nanoflakes, where the thickest nanoflake stack appears as the brightest. As seen from Fig. 1b,e, within the region of brightest PL, the pan-CL image has two main emission ‘hotspots’. We collect spectral signatures from each region, with representative smoothed-point spectra shown in Fig. 1f. We find that the CL spectrum of region 1 matches well with the PL spectrum, whereas region 2 has a broad spectral peak at 420 nm that is prevalent throughout this flake, as well as in many additional flakes. The ZPL in region 1 has a broader FWHM in the CL spectrum (10 nm) than in the PL spectrum (6 nm), which is probably a consequence of the CL spectrometer resolution (~ 10 nm). In addition to the ZPL, two other CL peaks are seen at 614 and 633 nm; as will be shown later, the first is from another nearby defect while the second is probably a phonon side band.

Cathodoluminescence mapping of individual emitters

We zoom into region 1 of Fig. 1e and use hyperspectral CL imaging to map local emission with ~ 15 -nm spatial resolution. Figure 2a shows a zoomed-in HAADF image of region 1. CL spectra are collected in 5-nm spatial increments throughout the region denoted by the white dotted box. The spectral images are analysed with non-negative matrix factorization³¹ (see Methods). The resultant three principal CL spectra and their corresponding spatial weight maps are included in Fig. 2a. As can be seen, one constituent spectrum exhibits a 582-nm ZPL, shown by the red spectrum and the red-coloured spectral weight map (labelled c_1); this is the single-photon emitter for which PL and CL closely match. Two additional emitters are located within 30 and 80 nm of this central emitter, respectively: one emitter is near the top of the mapped region, with a peak emission at 614 nm (purple map, c_2), while the other is near the bottom right, with a peak emission at 600 nm (blue map, c_3).

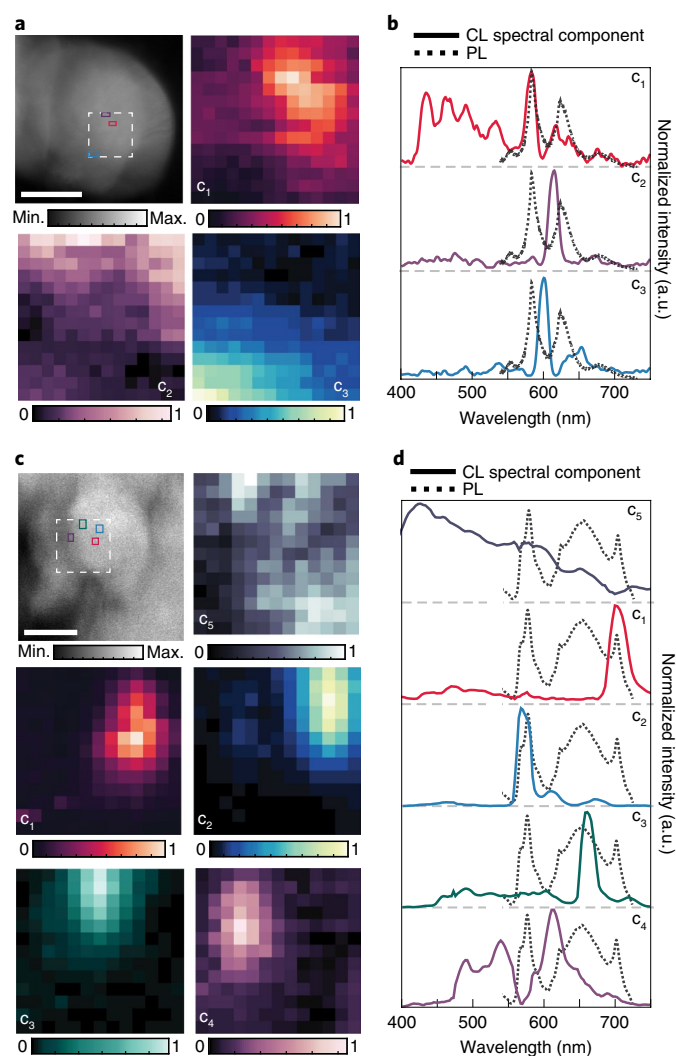


Fig. 2 | Cathodoluminescence mapping reveals multiple and distinct quantum-emitter species within a diffraction-limited optical spot.

a, STEM-HAADF image of region 1 in Fig. 1e and cathodoluminescence spectral weights (normalized to each component) of the white marked region. Scale bar in the HAADF image is 100 nm and each pixel in the CL spectral map is 5 nm. The red, purple and teal coloured boxes in the HAADF image are positions of the brightest pixels of the spectral components. **b**, The decomposed CL component spectra (solid lines, normalized to individual component) and normalized PL spectrum (black dotted lines) of the corresponding region. **c,d**, CL spectral maps and spectral components of another region hosting multiple quantum emitters. The PL spectrum contains two quantum emitters at 571 and 704 nm, but is a result of four spatially and spectrally distinct defects as seen in **d**. Pixel size in the CL map is 14.8 nm and the scale bar in the HAADF image is 200 nm.

Notably, even though the PL spectrum seems to only show a ZPL and its phonon side band, the CL spectrum actually shows another emitter at 614 nm, near the phonon side band peak. The centroid of each emitter is shown boxed on the HAADF image, and its intensity is due to variations in sample thickness. A change of thickness or contrast indicates a flake edge; our analysis (Supplementary Section 7) indicates that the SPE is at least 17 nm away from any flake edge, where the 600-nm emitter can be situated at an edge. Across 15 different SPEs with clear HAADF image contrast, we find five that are at least 12 nm away from any flake edges and nine that are within 5 nm of the edges.

The spectrum c_1 in Fig. 2a also illustrates a recurring emission profile, with four higher energy peaks at 433, 461, 490 and 532 nm. Such CL emission is recurrent in three spatially distinct emitters, with PL emission profiles consisting of a ZPL (near 578–590 nm) and a possible phonon replica doublet (Extended Data Fig. 1). In all three cases, the two highest energy peaks (433 and 461 nm) are separated by ~ 180 meV, which is nearly the value of the hBN phonon energy. Such CL spectra could emerge from closely spaced (sub-20 nm) emitters and their phonon side bands. The recurrent nature of the higher energy peaks suggests that such emitter(s) at 490 and 532 nm commonly accompany the 580 nm emitter.

PL spectra can also, in some cases, result from multiple single-photon emitters within one diffraction-limited spot. Figure 2b illustrates one such case. As can be seen, the PL spectrum (black dotted line) exhibits two distinctive, sharp peaks at 571 and 704 nm ($g^{(2)}$ in Supplementary Fig. 3). Through hyperspectral CL mapping we see that the two emission lines are actually from two different emitters, which are separated by 50 nm, shown in the blue and red CL maps, respectively. The smaller PL peak at 625 nm is probably a combination of the 570-nm-emitter phonon side band (blue solid spectrum with a small peak at 620 nm) and an additional radiative defect active only in the CL emitting spectrum at 625 nm (purple map). A fourth point defect at 682 nm is also evident upon electron-beam excitation, as shown in the green map. Finally, we observe a broad emission peak at 430 nm, which is a signal present in most flakes and which is generally very delocalized. This broad ultraviolet emission can be associated with prevalent impurity atoms, such as carbon; previously, blue PL after ultraviolet excitation has also been linked to carbon centres³². Thus, hyperspectral CL mapping allows the delineation of PL spectra, to further reveal the existence of multiple optically active defects that are masked by a combination of their spatial positions with respect to each other and the diffraction limit.

The spectral maps in Fig. 2 also provide an estimate of the carrier diffusion lengths. Line scans of intensity across particular defect centres are plotted in Supplementary Fig. 9. We find that the emission intensity decreases to $1/e$ of its maximum value at 15–60 nm for various emitters, which enables us to distinguish emitters with similar resolution. As discussed in the Supplementary Information, the high density of structural defects and dislocations near emitters may account for such short diffusion lengths.

Using our spectral mapping technique, we build a library of PL–CL signatures for 40 stable emitters across 15 different samples. Figure 3 presents examples of the PL and CL responses where PL spectra are reproducible after electron-beam imaging (examples in Supplementary Section 8). Two distinct behaviours are observed: one class of emitters exhibits PL emission lines that are well matched to CL emission lines (Fig. 3a), while the second class has a CL signature that is shifted from the PL signature (Fig. 3b). In this second class, some emitters possess only a slight CL–PL shift, while others show negligible visible-frequency CL. The first class of emitters exhibits ZPLs predominately around 545 nm and 580–630 nm. Certain emitters with ZPLs near 550 and 570 nm and above 700 nm exhibit a 10–15-nm CL–PL spectral shift (that is, E_{12} , E_{13} , E_2 , E_4 , E_9 , E_{14} , E_{17} and E_{18}). Possibly, the orbital wavefunction of such emitter energy levels is more sensitive to external stimuli, including electron beam-induced charging, carrier screening or the local temperature. Finally, we observe certain emitters with ZPLs in the range 650–700 nm with negligible CL beyond 550 nm (that is, E_{19} , E_{20} and E_{24} in Supplementary Fig. 11). Such a large shift (>450 meV) between the PL and CL ZPLs could be due to a change in the emitter charge state¹¹, or to a nearby emitter that is not excited by 532-nm light but that captures carriers competitively in the CL process.

Nanoscale strain mapping

We can correlate emitter optical emission with the emitter's local in-plane strain using nanobeam electron diffraction (NBED).

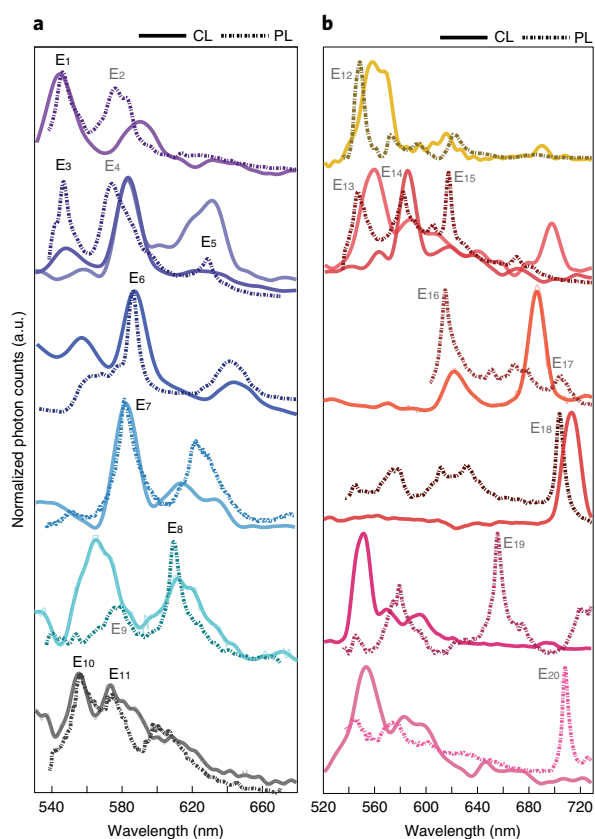


Fig. 3 | Correlating stable emitter PL and CL spectra reveals two types of behaviour. **a,b**, Correlated PL (dotted lines) and CL (solid lines) spectra of 20 emitters from 12 different regions are plotted and overlaid. Most emitters in **a** (names in black font) have closely matched ZPLs upon optical and electron-beam excitation. Emitters in **b**, and E_2 and E_4 , have variable spectral shifts between their PL and CL ZPLs.

We collect diffraction images every 1–3 nm across the emitter hotspot (see Supplementary Section 3) and reconstruct in-plane strain maps by fitting the positions of the diffraction discs in each image. The change in lattice distance at each point is calculated by comparing to a reference distance to measure the strain. When many flakes stack together, as is common in our samples, we focus exclusively on regions without any lateral rotation between flakes (that is, containing only one set of diffraction discs). Notably, this strain is experienced by the entire stack of hBN flakes. In Fig. 4a, the emitter E_7 CL hotspot is marked by a black rectangle in the HAADF image. The PL and CL of the emitter can be seen in Fig. 4b. Diffraction images are collected in the red dotted rectangular region; an averaged diffraction image is shown in Fig. 4c. The strain maps along $\langle 10\bar{1}0 \rangle$ and $\langle \bar{1}2\bar{1}0 \rangle$ directions are presented in Fig. 4d, where the position of the brightest pixel of the CL map is marked with a black rectangle. For this particular emitter, a large strain variation in the CL hotspot is observed compared to the surrounding area: from -2.4% to 2.2% along the u direction and from 0 to -2% along the v direction. On the other hand, as shown in Fig. 4e–h, we observe the emitter E_8 at 610 nm in a relatively unstrained region, indicating that strain is not a precursor for emitter formation. To compare strain values across emitters, we fit each region with 2–3 different orthogonal pairs of u and v vectors and calculate the mean and standard deviations of the CL hotspot strain values over those fittings. More examples can be found in Supplementary Figs. 4 and 5.

Classification of distinct emitter species

Figure 5 summarizes the mean and standard deviation of strain values in the CL hotspots for ten emitters along two crystal directions. We can distinguish between distinct emitter species from these strain variations combined with their CL–PL responses, as summarized in Fig. 5a–c. Our results indicate that at least four classes of emitters exist. First, we observe one type of defect near 580 nm (E_{11} , E_7 and E_6). These emitters have matched PL–CL spectra but large strain variations amongst them. The observed spectral tunability (121 meV) in this class of emitters can be due to strain, which is consistent with previous reports^{10,33} and our first-principle modelling (see Supplementary Section 10). Taking E_6 as an unstrained emitter and $N_B V_N$ (an anti-site defect complex where nitrogen occupies a boron site and a vacancy occupies the nitrogen site) as the most probable candidate, the grey arrow shows the calculated tuning of the emission wavelength, assuming 1% strain along each direction. We note that emitter E_{10} at 554 nm could be part of this same class, even though the strain variation is not more than 1.5% compared to E_6 ; similar emitters can be seen in Fig. 5c. We hypothesize that the CL–PL spectral shifts of 10–13 nm (~ 40 meV) observed in the red emitters in Fig. 5 could originate from charging effects due to the electron beam, since an emitter positioned nearer to the carbon substrate will experience a different charging level to one positioned near the middle or top of a hBN flake.

Next, we see that the three emitters around 615 nm originate from another distinct defect species, which we term type ii. Notably, the type i emitter E_6 (582 nm) and type ii emitter E_8 (610 nm) are separated by 100 meV, with negligible strain difference, making it unlikely that the 615-nm emitters are strain-tuned versions of type i emitters. The arrow in this region indicates the calculated emission tuning of the nominally unstrained emitter E_8 due to 1% strain along each direction.

We identify a third class of emitters around 705 nm. These emitters have shifted CL–PL spectral responses and are shifted from the 630 nm emitter E_{21} by 200 meV in energy, with at most a 1% strain difference. Such large spectral separation with small strain difference exceeds theoretically predicted spectral tunability with strain for known defects and defect complexes (see Supplementary Fig. 13 and refs. 10,33). More examples of such type iii emitters in Fig. 5c also show, predominantly, shifted spectral responses between their PL and CL ZPLs.

Finally, the emitters around 660 nm either have very low quantum efficiency under electron-beam excitation or have a much larger shift (>450 meV) in their CL responses (E_{19} , E_{20} in Fig. 3). Given their very different spectral responses (and hence an uncertainty in the TEM–CL about the precise emitter location), we could not characterize their host region strain. Still, given their largely shifted PL–CL spectra, we can postulate that they are a distinct defect species (type iv). These results are consistent with ref. 34, which hypothesized a distinct defect nature for the 650 and 580 nm emitters.

We can combine our experimental results, first principles modelling and the community’s understanding of hBN defect structures to interpret our results. Possible colour centres in hBN are boron monovacancies (V_B), its hydrogen and oxygen complexes, nitrogen monovacancies (V_N) and $C_B V_N$, $N_B V_N$ and $O_{2B} V_N$ (see Supplementary Section 10 and ref. 20). The calculated knock-on threshold energies to eject B and N in monolayer hBN are 80 and 118.6 kV, respectively³⁵. Therefore, with our electron accelerating voltage of 80 kV, we do not expect the monoboron vacancies (V_B) to be stable. In particular, under 80–120 kV electron-beam irradiation, V_B has only been observed to form in mono- and bilayer hBN, and once a monovacancy is formed it selectively grows into larger triangles^{25,35,36}. Similarly, V_N is not predicted to be a stable single-photon emitter and is not active at visible-light frequencies. Therefore, our stable defects that have reproducible CL and PL are not these monovacancy defects.

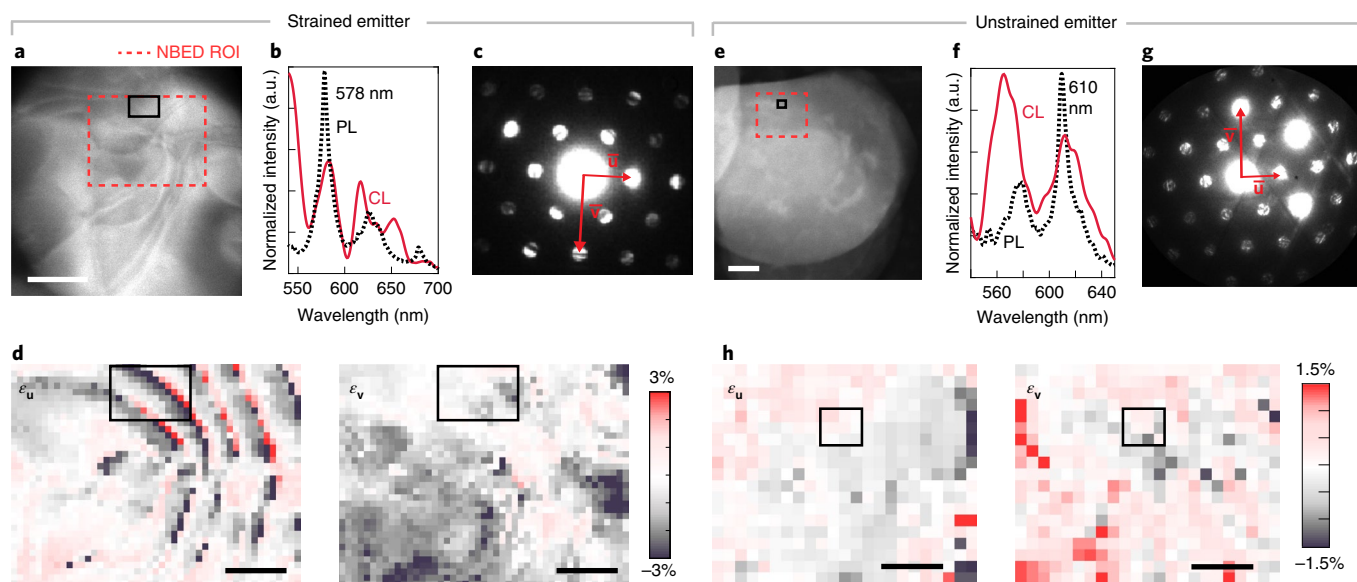


Fig. 4 | Correlating quantum emission with local strain. **a, b**, HAADF image (**a**) and corresponding PL and CL spectra (**b**) of one emitter with a 578 nm ZPL. Red dotted rectangle is the region of interest (ROI) for NBED mapping. **c**, Averaged NBED diffraction pattern showing one set of u and v vectors for calculating strain. **d**, Reconstructed strain maps for the NBED ROI in **a**. **e, f**, HAADF image (**e**) and corresponding PL and CL spectra (**f**) of another region with an emitter at 610 nm. **g, h**, Corresponding NBED diffraction image (**g**) and in-plane strain maps (**h**) along two directions. Both direction maps show negligible strain in the optically bright pixels. Scale bars, 50 nm for HAADF images; 20 nm for strain maps. The localization of the CL bright spot to the strain map (black rectangle) has, at most, a 6-nm drift error in both the x and y directions (Supplementary Section 6).

Instead, our type i–iv emitters probably emerge from $C_B V_N$, $N_B V_N$ and $O_{2B} V_N$ and complexes of these defects, as well as V_N with interstitials (B_i , O_i , C_i)³⁷. For example, V_N has been postulated to be a donor defect^{26,38}, and a change of its charge state can result in a distinct CL peak from its PL peak; our type iv defects with no visible-frequency CL but strong SPE emission in PL could be a complex with this donor. In particular, electron beam-induced charging can locally modify the potential landscape and hence the defect charge state. This result parallels the disappearance and reappearance of charged defects in bulk hBN due to probe-assisted carrier tunneling, as seen by Wong and colleagues²⁶.

In summary, we have established a direct correlation between PL, CL and local crystallographic strain of quantum emitters in hBN. The combined results of these correlated measurements indicated that at least four distinct classes of defects are responsible for quantum emission in hBN. CL hyperspectral mapping reveals multiple emitters within a diffraction-limited optical spot, each contributing to the PL spectra. The large spectral variability of single-photon emitters is not due solely to strain. Additionally, strain is not required to activate the emission, nor are defects required to be located at the edges of the flakes. Importantly, most of the emitters in multilayer films are stable upon electron and optical irradiation—a crucial feature for future atomic-scale imaging. Looking forward, we envision ångström-scale imaging of a variety of two-dimensional materials will reveal the rich photonic properties that emerge with atomic-scale architecture and ‘defects by design’.

Online content

Any methods, additional references, Nature Research reporting summaries, source data, extended data, supplementary information, acknowledgements, peer review information; details of author contributions and competing interests; and statements of data and code availability are available at <https://doi.org/10.1038/s41563-020-0616-9>.

Received: 21 January 2019; Accepted: 16 January 2020;
Published online: 24 February 2020

References

- Kucsko, G. et al. Nanometre-scale thermometry in a living cell. *Nature* **500**, 54–58 (2013).
- Taylor, J. et al. High-sensitivity diamond magnetometer with nanoscale resolution. *Nat. Phys.* **4**, 810–816 (2008).
- Aslam, N. et al. Nanoscale nuclear magnetic resonance with chemical resolution. *Science* **357**, 67–71 (2017).
- Wehner, S., Elkouss, D. & Hanson, R. Quantum internet: a vision for the road ahead. *Science* **362**, eaam9288 (2018).
- Liao, S.-K. et al. Satellite-to-ground quantum key distribution. *Nature* **549**, 43–47 (2017).
- Awschalom, D. D., Hanson, R., Wrachtrup, J. & Zhou, B. B. Quantum technologies with optically interfaced solid-state spins. *Nat. Photonics* **12**, 516–527 (2018).
- Atature, M., Englund, D., Vamivakas, N., Lee, S.-Y. & Wrachtrup, J. Material platforms for spin-based photonic quantum technologies. *Nat. Rev. Mater.* **3**, 38–51 (2018).
- Tran, T. T., Bray, K., Ford, M. J., Toth, M. & Aharonovich, I. Quantum emission from hexagonal boron nitride monolayers. *Nat. Nanotechnol.* **11**, 37–41 (2016).
- Jungwirth, N. R. et al. Temperature dependence of wavelength selectable zero-phonon emission from single defects in hexagonal boron nitride. *Nano Letters* **16**, 6052–6057 (2016).
- Grosso, G. et al. Tunable and high-purity room temperature single-photon emission from atomic defects in hexagonal boron nitride. *Nat. Commun.* **8**, 705 (2017).
- Sontheimer, B. et al. Photodynamics of quantum emitters in hexagonal boron nitride revealed by low-temperature spectroscopy. *Phys. Rev. B* **96**, 121202 (2017).
- Exarhos, A. L., Hopper, D. A., Grote, R. R., Alkauskas, A. & Bassett, L. C. Optical signatures of quantum emitters in suspended hexagonal boron nitride. *ACS Nano* **11**, 3328–3336 (2017).
- Martínez, L. et al. Efficient single photon emission from a high-purity hexagonal boron nitride crystal. *Phys. Rev. B* **94**, 121405 (2016).
- Tran, T. T. et al. Robust multicolor single photon emission from point defects in hexagonal boron nitride. *ACS Nano* **10**, 7331–7338 (2016).
- Choi, S. et al. Engineering and localization of quantum emitters in large hexagonal boron nitride layers. *ACS Appl. Mater. Interfaces* **8**, 29642–29648 (2016).
- Chejanovsky, N. et al. Structural attributes and photodynamics of visible spectrum quantum emitters in hexagonal boron nitride. *Nano Lett.* **16**, 7037–7045 (2016).
- Jungwirth, N. R. & Fuchs, G. D. Optical absorption and emission mechanisms of single defects in hexagonal boron nitride. *Phys. Rev. Lett.* **119**, 057401 (2017).

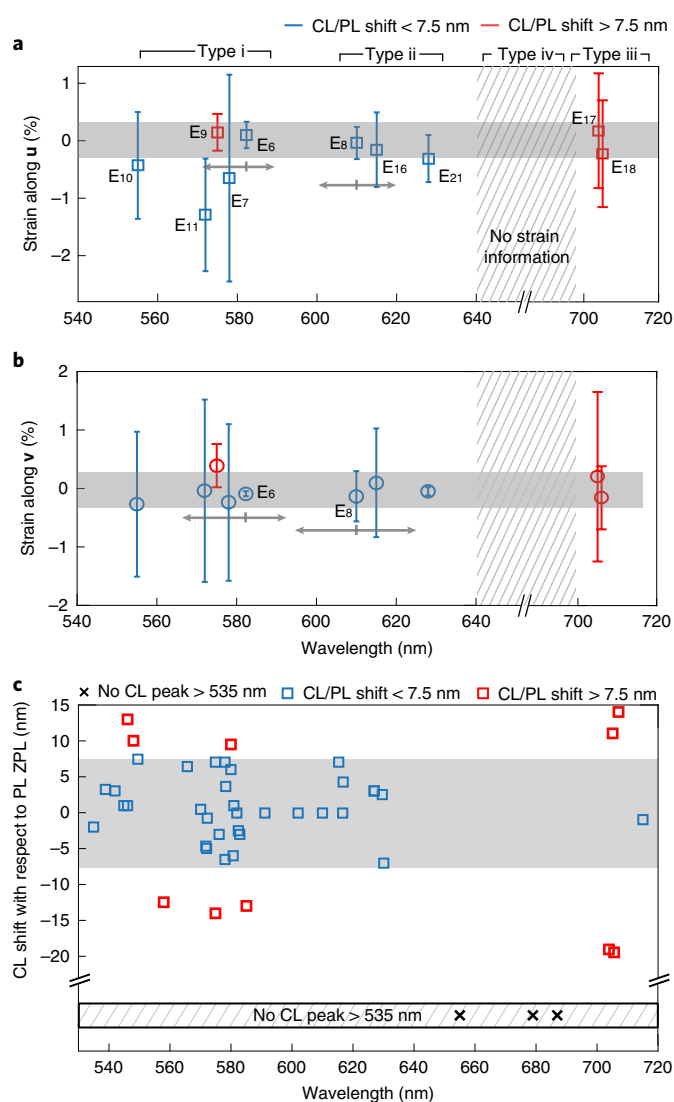


Fig. 5 | Emitter classification. **a, b**, Average strain and standard deviation in the CL hotspot along the **u** and **v** directions as a function of emitter emission wavelengths for ten emitters across eight different regions of six samples. The hatched regions near 650 nm indicate a spectral region where the emitters do not have any visible-region CL (examples: E_{19} – E_{20} in Fig. 3b). **c**, CL spectral shift from the PL ZPL. The grey shaded region corresponds to 1.5 \times the CL spectrometer resolution; therefore, any emitter within this region is taken to have the same CL–PL ZPL and is plotted in blue in all three panels. The emitters with larger spectral shifts between PL and CL are plotted in red. Black crosses represent emitters that either do not have strong CL peaks or emit in the ultraviolet.

18. Schell, A. W., Svedendahl, M. & Quidant, R. Quantum emitters in hexagonal boron nitride have spectrally tunable quantum efficiency. *Adv. Mater.* **30**, 1704237 (2018).
19. Reimers, J. R., Sajid, A., Kobayashi, R. & Ford, M. J. Understanding and calibrating density-functional-theory calculations describing the energy and spectroscopy of defect sites in hexagonal boron nitride. *J. Chem. Theory Comput.* **14**, 1602–1613 (2018).
20. Tawfik, S. A. et al. First-principles investigation of quantum emission from hBN defects. *Nanoscale* **9**, 13575–13582 (2017).
21. Feng, J. et al. Imaging of optically active defects with nanometer resolution. *Nano Lett.* **18**, 1739–1744 (2018).
22. Bourrellier, R. et al. Bright uv single photon emission at point defects in h-bn. *Nano Lett.* **16**, 4317–4321 (2016).
23. Meuret, S. et al. Photon bunching in cathodoluminescence. *Phys. Rev. Lett.* **114**, 197401 (2015).
24. Alem, N. et al. Atomically thin hexagonal boron nitride probed by ultrahigh-resolution transmission electron microscopy. *Phys. Rev. B* **80**, 155425 (2009).
25. Jin, C., Lin, F., Suenaga, K. & Iijima, S. Fabrication of a freestanding boron nitride single layer and its defect assignments. *Phys. Rev. Lett.* **102**, 195505 (2009).
26. Wong, D. et al. Characterization and manipulation of individual defects in insulating hexagonal boron nitride using scanning tunnelling microscopy. *Nat. Nanotechnol.* **10**, 949–953 (2015).
27. Lin, W.-H. et al. Atomic-scale structural and chemical characterization of hexagonal boron nitride layers synthesized at the wafer-scale with monolayer thickness control. *Chem. Mater.* **29**, 4700–4707 (2017).
28. Barja, S. et al. Identifying substitutional oxygen as a prolific point defect in monolayer transition metal dichalcogenides. *Nat. Commun.* **10**, 3382 (2019).
29. Cassabois, G., Valvin, P. & Gil, B. Hexagonal boron nitride is an indirect bandgap semiconductor. *Nat. Photonics* **10**, 262–266 (2016).
30. Koperski, M., Nogajewski, K. & Potemski, M. Single photon emitters in boron nitride: more than a supplementary material. *Opt. Commun.* **411**, 158–165 (2018).
31. de la Peña, F. et al. *hyperspy/hyperspy* v.1.4.1 (Zenodo, 2018); <https://doi.org/10.5281/zenodo.1469364>.
32. Katzir, A., Suss, J., Zunger, A. & Halperin, A. Point defects in hexagonal boron nitride. I. EPR, thermoluminescence, and thermally-stimulated-current measurements. *Phys. Rev. B* **11**, 2370 (1975).
33. Xue, Y. et al. Anomalous pressure characteristics of defects in hexagonal boron nitride flakes. *ACS Nano* **12**, 7127–7133 (2018).
34. Vogl, T., Doherty, M. W., Buchler, B. C., Lu, Y. & Lam, P. K. Atomic localization of quantum emitters in multilayer hexagonal boron nitride. *Nanoscale* **11**, 14362–14371 (2019).
35. Kotakoski, J., Jin, C., Lehtinen, O., Suenaga, K. & Krasheninnikov, A. Electron knock-on damage in hexagonal boron nitride monolayers. *Phys. Rev. B* **82**, 113404 (2010).
36. Meyer, J. C., Chuvilin, A., Algara-Siller, G., Biskupek, J. & Kaiser, U. Selective sputtering and atomic resolution imaging of atomically thin boron nitride membranes. *Nano Lett.* **9**, 2683–2689 (2009).
37. Weston, L., Wickramaratne, D., Mackoite, M., Alkauskas, A. & Van de Walle, C. G. Native point defects and impurities in hexagonal boron nitride. *Phys. Rev. B* **97**, 214104 (2018).
38. Yin, L.-C., Cheng, H.-M. & Saito, R. Triangle defect states of hexagonal boron nitride atomic layer: density functional theory calculations. *Phys. Rev. B* **81**, 153407 (2010).

Publisher's note Springer Nature remains neutral with regard to jurisdictional claims in published maps and institutional affiliations.

© The Author(s), under exclusive licence to Springer Nature Limited 2020

Methods

Sample preparation. Nanoflakes of hBN (2.5 μl) (each flake 1–5 monolayers) in ethanol–water solution (Graphene Supermarket) were drop-cast onto cleaned holey carbon TEM grids (Quantifoil 0.6/1). The samples were dried in a vacuum bell jar at 80 °C for 30 min and annealed for 2 h under ambient pressure and environment at low temperature (200–220 °C) due to the stability of the ultrathin carbon TEM substrate. Samples were stored in a glovebox under argon.

Optical characterization. The photoluminescence maps of the hBN nanoflakes were acquired using a Horiba confocal Raman microscope, with a $\times 100$ objective (numerical aperture, 0.6), an excitation laser power of $\sim 100 \mu\text{W}$ at 532 nm and a grating of 600 lines per mm groove density. The typical laser spot size was $\sim 600 \text{ nm}$ and the acquisition time was 1 s for each spectrum.

Autocorrelation $g^{(2)}$ measurements. Second-order autocorrelation measurements were performed using a Hanbury Brown–Twiss set-up. The quantum emitter (QE) was excited by a 532-nm continuous wave laser through a laser line filter, and the photoluminescence from the QE was filtered with a dichroic filter (Semrock FF552-Di02-25 $\times 36$) and a bandpass filter (bandwidth of 10 nm) centred around the QE emission wavelength, and collected by a multimode fibre. The photoluminescence was directed towards a fibre beam splitter; at the two output ports of the beam splitter were two single-photon counting modules (SPCMs, PerkinElmer SPCM-AQR-14-FC). One SPCM was used as a start signal and the second was used as a stop signal. By measuring the time delay between the two successive photon arrivals, a histogram of occurrences as a function of time delay was constructed. The photon counts were correlated using a PicoHarp300 time-correlated SPCM, with a count rate of 10k counts per second and a typical integration time of 20 min for one dataset. For this measurement, the excitation laser power was kept below $20 \mu\text{W}$ to prevent degradation of both the emitters and the thin carbon film ($\sim 12 \text{ nm}$) TEM grid. The counts were normalized by counts at $4 \mu\text{s}$ and fitted assuming a three-level system (more in Supplementary Section 2).

STEM–CL characterization. The FEI Titan electron microscope was operated at 80 kV. The Gatan Vulcan Cathodoluminescence TEM holder was used for light collection in STEM. The holder has two mirrors positioned above and below the sample. A hole of about $500 \mu\text{m}$ in the mirrors allows the electron beam through. The reflected light was focused onto two optical fibres (multimode step index) and directed onto the PMT for panchromatic mapping or to the grating and CCD (cooled to $-60 \text{ }^\circ\text{C}$) for spectral mapping. The collection window of the two mirrors in the CL holder was $200 \mu\text{m}$ in diameter. We used two fibre-coupled (multimode) light-emitting diodes (red and green) to align the two hotspots from the two mirrors after loading the sample.

The panchromatic photon pulse counting maps using the PMT were collected as 512×512 pixels and each pixel acquisition time was $60/100 \mu\text{s}$. For this mapping, the C2 aperture was chosen to be $70 \mu\text{m}$ (convergence semi-angle is 14 mrad) and the STEM spot size (non-monochromated) was chosen as either 6 or 7 (depending on the emitter intensity) and the screen current was 20 pA (spot size 7) or 40 pA (spot size 6). The spectral maps were collected using a grating with 150 lines per mm and an acquisition time of 4–8 s per pixel, again depending on the intensity of the particular emitter. The spot size for this mapping was 6 and screen current was 40 pA. Software drift correction (after every three rows) was on during the collection. Samples were usually very stable with minimal drift. Dark corrections were performed at the end of collection for each map. All mapping was done at room temperature.

Correlation of optical and electron micrographs. The TEM substrate was supported by a gold grid where each square in the grid was $40 \times 40 \mu\text{m}^2$. We focus on the central four squares, as these can be positioned to be in the CL holder optical hotspot ($\sim 200 \mu\text{m}$ in diameter). The four corners of each square served as alignment markers for the region of interest; we noted coordinates of each corner and each emitter region to triangulate distances from each corner. We took optical images of the entire square with a $\times 100$ objective and marked these regions with

respect to the corners. Before STEM–CL imaging, we obtained TEM images at $\times 70$ to $\times 100$ magnification (LM mode). We then used previously calculated distances from the corners and the $\times 100$ optical image to locate the regions of interest; this method was accurate to $1\text{--}2 \mu\text{m}$. For higher accuracy mapping, we used a numbering system for the holes (that is, recording the number of holes in the x and y direction from any specific corner) to determine the appropriate position in the TEM. For localization beyond the diffraction limit, we collected STEM pan-CL maps as described in Fig. 1e. This method allowed us to determine how many ‘bright’ emitters were located inside the $\sim 500 \text{ nm}$ optical PL hotspot. Next, we collected spectral signatures of each bright region as described in the main text.

NBED diffraction experiment. The C2 aperture size was chosen as $10 \mu\text{m}$ (convergence semi-angle of 2 mrad), the spot size was 11, the screen current was $\sim 1 \text{ pA}$, each pixel acquisition time was 0.1 s and each diffraction image was $4\text{k} \times 4\text{k}$.

CL spectral decomposition. Spectral decomposition was performed using the HyperSpy package in Python³¹. Any noise peaks were removed and the spectra were smoothed with the LOWESS/LOESS weighted regression algorithm using a smoothing parameter of 0.04. We performed principal component analysis (PCA) on the dataset to estimate the number of spectral components from the PCA weights. Finally, non-negative matrix factorization was performed with this number of spectral components to calculate the spectral weights.

Data availability

All strain analysis data presented in Fig. 5 are included in Supplementary Information. Due to large file sizes, strain mapping and all other electron microscopy source data are available from the corresponding authors on request.

Acknowledgements

The authors acknowledge useful discussions about strain mapping with T. Pekin (Humboldt-Universität zu Berlin) and about CL–PL correlations with C. McLellan (Stanford). TEM imaging and spectroscopy were performed at the Stanford Nano Shared Facilities and Stanford Soft & Hybrid Materials Facility. The PL, TEM experiments and theoretical modelling were supported by the DOE ‘Photonics at Thermodynamic Limits’ Energy Frontier Research Center under grant no. DE-SC0019140. F.H. gratefully acknowledges the support of the Diversifying Academia, Recruiting Excellence (DARE) Doctoral Fellowship Program by Stanford University. J.V. acknowledges the support the NSF Quantum Leap EAGER grant no. DMR 1838380. T.F.H. and L.Y. also acknowledge support from the Betty and Gordon Moore Foundation EPIQS Initiative through grant no. GBMF4545.

Author contributions

F.H., L.Y., T.F.H. and J.A.D. conceived the project. F.H. made the samples and performed the PL and TEM experiments. J.L.Z., L.Y. and F.H. performed the second-order correlation measurements under the supervision of J.V. C.J.C. and P.N. performed the theoretical calculations. A.F.M. assisted in strain map data collection. M.N. and I.A. assisted in sample preparation. F.H. and J.A.D. wrote the draft. J.A.D. supervised the project. All co-authors discussed the results and provided useful feedback on the manuscript.

Competing interests

The authors declare no competing interests.

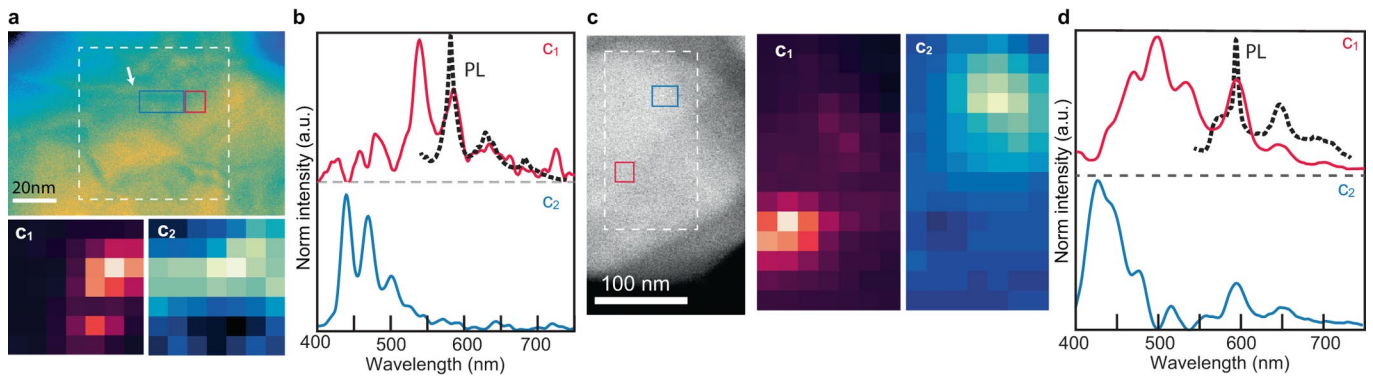
Additional information

Extended data is available for this paper at <https://doi.org/10.1038/s41563-020-0616-9>.

Supplementary information is available for this paper at <https://doi.org/10.1038/s41563-020-0616-9>.

Correspondence and requests for materials should be addressed to F.H. or J.A.D.

Reprints and permissions information is available at www.nature.com/reprints.



Extended Data Fig. 1 | Higher energy lines associated with the 580-590 nm emitters. **a**, HAADF and decomposed CL spectral weight maps of the emitter with ZPL at 578 nm in Fig. 4a of main text. **b**, CL spectral components showing higher energy peaks similar to that in Fig. 2a. **c**, HAADF and CL spectral weight maps of the emitter E6 in Fig. 3a with ZPL at 590 nm. **d**, CL spectral components for emitter in (c). Each pixel in the CL weight maps is 15 nm. For both emitters here, the PL spectrum has two probable phonon-sidebands, a similar spectral signature to the emitter in the main text Fig. 2a. All these three emitters have four higher energy (UV-blue) peaks in their CL spectrum. For the particular emitter in panels (c-d), spectral decomposition shows that the 420 nm emitter is located 80 nm away from the 590 nm emitter. However, the 460 nm, 500 nm and 532 nm peaks are localized to the same 15 nm bright pixel as the 590 nm peak.